**Published article:**

Hondow, N and Fuller, RO (2014) *The use of preformed nanoparticles in the production of heterogeneous catalysts.* Journal of Colloid and Interface Science, 417. 396 - 401. ISSN 0021-9797

http://dx.doi/10.1016/j.jcis.2013.11.064

# The use of preformed nanoparticles in the production of heterogeneous catalysts

Nicole Hondow[a] and Rebecca O Fuller[b*]

[a] Institute for Materials Research, School of Process, Environmental and Materials Engineering, University of Leeds, Leeds LS2 9JT, UK.

[b] School of Chemistry and Biochemistry M310, The University of Western Australia, Crawley WA 6009, Australia.

Corresponding author:* Dr Rebecca Fuller
School of Chemistry and Biochemistry, M310
The University of Western Australia
35 Stirling Hwy
Crawley, WA 6009 Australia
Tel:+61-8-6488-4489
Fax:+61-8-6488-7247
E:rebecca.fuller@uwa.edu.au

## Abstract

Preformed iron oxide nanoparticles have been successfully assembled onto alumina and MCM-41 support materials. The particles are found to disperse evenly over the surface of the silicate; however, in the case of the alumina we find that in addition to areas of even distribution there is also some clustering of the particles. The materials are stable under heat treatment, with no signs of further aggregation during calcination. We investigate the reducibility of the materials through $H_2$-TPR studies and we find that the particles are reducible around 500-550 $^{o}$C. The reduction process is complete at temperatures where MCM-41 can undergo degradation, supporting that the alumina based materials are more suited to the multiple base oxidation reduction steps in the catalytic cycle.

## Keywords

Nanoparticles; iron oxide; MCM-41; supported; alumina; Fischer-Tropsch

## 1. Introduction

The use of nanoparticles as Fischer-Tropsch (FT) catalysts has attracted increasing interest in recent times. [1-3] This has largely arisen out of their size dependent properties, ease of preparation for FT active metals and large number of atoms at their surface. Despite the development in a number of chemical approaches [4] that give control over particle size and composition, and the subsequent assemblage of these preformed particles onto supports, [5] very few literature examples involving the addition of preformed nanoparticles to support materials exist. [3, 6, 7] This method is highly advantageous as it allows greater control over what species are assembled onto a support material and it removes the dispersion problems seen with metal clusters in traditional FT catalysts.[8] Further research is required to develop new systems based on the assemblage of preformed particles onto supports so that an assessment of the benefits of these materials can be made. This work involves the development of such new systems.

One of the main advantages offered by using preformed nanoparticles over those formed in-situ using co-precipitation and sol-gel is the ability to easily access the size dependent properties of the catalyst for the generation of particular alkanes. Producing narrow range of particle sizes for FT containing metals is easily achieved using hydrothermal high temperature reactions.[9, 10] Co-precipitation and sol-gel methods that are used in industrial processes result in particles that tend to be less homogeneous in both size and composition.[11] Often these materials also have stability issues arising from the leaching of the deposited metal species at the elevated temperatures required for metal reduction.[12] Some balance needs to be achieved between the simple precursors, scale and simple purification techniques offered by co-precipitation and sol-gel with the structural control and stability seen in the preformed nanoparticles systems.

FT active metals generally involve iron, cobalt, nickel and ruthenium due to the preference in production of diesel fuel and linear, high molecular weight alkanes. Cobalt catalysts are the most developed FT catalyst as syngas is normally derived from natural gas, which has a higher hydrogen/carbon monoxide ratio and relatively low sulfur content. Although there have been relatively few reports of the use of preformed Co nanoparticles, many examples exist on size effects for relatively monodisperse Co containing nanoparticles.[13-17] Despite our own work,[5, 7] few iron based preformed particle systems have been explored. Iron based catalysts are preferred for low grade feedstocks based on coal. Synthesis gas in this case has a higher sulfur content and a low $H_2$/CO ratio due to their higher water-gas-shift activity. Iron is advantageous, due to its relatively low costs and higher FT activity. Furthermore, the synthesis of iron based systems via hydrothermal methods is well established in the literature [4, 18, 19] and preformed particles have been shown to be readily incorporated into Mobil Composition of Matter (MCM) materials during their synthesis.[20] Iron based nanoparticles are advantageous over their cobalt counterparts as not only are their syntheses more developed for commercialisation, but also because they offer a more accessible range of bimetallic systems. With the exception of cobalt ferrite,[21] complexities tend to arise in cobalt nanoparticle synthesis because cobalt possesses multiple crystal structures that are close in energy. Hence subtle changes in temperature or surfactant lead to much more dramatic effects in surface chemistry, resultant size and shape of nanoparticles formed in comparison to iron.[22] Based on this we have explored the ability to assemble preformed iron oxide particles onto supports.

In this paper we examine the assemblage of preformed iron oxide nanoparticles, onto two support materials, a mesoporous silica, MCM-41, and an alumina, puralox SBa200.  These materials are ideal candidates for use as high temperature FT catalysts. We use a variety of characterization techniques to evaluate the assemblage of the preformed particles onto supports, determining if this methodology is accessible for other nanoparticles and supports or is limited to the previously studied FePt and MCM silicas.

## 2. Materials and Methods

### 2.1 Synthesis of iron oxide nanoparticles

Iron oxide nanoparticles were synthesized using the hydrothermal technique [18] involving the addition of $Fe(CO)_5$ (0.2 mL, 1.52 mmol, Strem Chemicals Inc.) to a 10 mL solution of octyl ether (Sigma Aldrich) with oleic acid (1.92 mL, 6.08 mmol Sigma-Aldrich) at 100 $^{O}$C. Following the rapid injection of the iron precursor the solution was heated to reflux at a rate of 10 degree/min. After 1 hour the reaction was cooled to room temperature where 0.34 g of anhydrous $(CH_3)_3NO$ (Sigma-Aldrich) was added and the solution heated to

130 $^{O}$C. After being maintained at this temperature for 2 hours the solution was returned to reflux and left for an additional hour. The solution was then cooled to room temperature and the particles purified by centrifugation with ethanol.

## 2.2 Assemblage of nanoparticles onto support materials

The particles were subsequently reacted with either a well ordered silicate (MCM-41), that had been prepared via a literature preparation [23] and then calcined at 550 $^{o}$C for 1 hour in $N_2$ and overnight in air (pore diameter ca. 27 Å BET 1030 $m^2/g$), or a commercially available alumina (SASOL puralox SBa200) that had been calcined for 2.5 hours at 750 $^{o}$C (pore diameter ca. 84 Å BET 161 $m^2/g$). The samples will be referred to Fe-MCM and Fe-puralox respectively. A typical procedure involved the addition of approximately 200 mg of nanoparticles suspended in 10 mL hexane to a solution of 2 g of support material in 20 mL hexane overnight. The process was deemed complete when the hexane became colorless. The pale brown/red powder (~2.17 g) was washed with more hexane and collected via filtration and dried under vacuum. Temperature stability of the catalysts was explored by calcination under two different thermal conditions. Temperatures of 200 $^{o}$C and 550 $^{o}$C were used, for a total of four hours. In each, the first hour was under a flow of nitrogen with a further three hours under a flow of air.

## 2.3 Characterization

Transmission electron microscopy (TEM) was conducted on three microscopes; a JEOL 3000F operating at 300 kV and equipped with a Gatan

Orius SC1000, an FEI Tecnai F20 operating at 200 kV and equipped with a Gatan Orius SC600 camera, and an FEI CM200 operating at 197 kV equipped with a Gatan GIF200. Compositional analysis in the TEM was performed using energy dispersive X-ray (EDX) spectroscopy (Oxford Instruments, JEOL 3000F and FEI Tecnai F20) and energy filtered TEM (EFTEM) (Gatan, CM200).

Powder X-ray diffraction (XRD) patterns were recorded at room temperature on a Siemens D5000 diffractometer with CuK$\alpha$ radiation generated at 40 kV and 35 mA. The amount of Fe, Al and Si in the calcined catalysts was determined by X-Ray Florescence (XRF) Spectrometry (Ultra Trace Pty Ltd.). Samples were cast using a 12:22 flux to form a glass bead that could be analysed by XRF.

$N_2$ absorption and desorption isotherms were measured at 77 K for both the calcined support materials and calcined catalysts using a TriStar II 3020. Prior to measurement the sample (~0.1 g) was degassed under vacuum overnight at 130 $^oC$. Specific surface areas were estimated using BET analysis and pore diameters by BJH desorption.

Thermal gravimetric analysis (TGA) was performed on the samples using a TA SDT Q600. The sample was initially dried at 105 $^oC$ for 10 min under a flow (50 mL/min) of air.  After cooling to ambient temperature measurements were carried out with a linear ramp to 1000 $^oC$ at 10 $^oC$/min with a flow of 8% $H_2$ in $N_2$ (50 mL/min).

The reductive behavior of the iron oxide supported catalysts was studied using a Micromeritics AutoChem II 2920 apparatus. Around 30 mg of calcined sample was initially flushed with Ar at 200 $^oC$ for half an hour. Subsequently the sample was cooled to ambient temperature and the gas was then switched to 8% $H_2$ in $N_2$ and the temperature increased up to 900 $^oC$. A downstream ice/salt trap was used to ensure any water produced was retained. The thermal conductivity detector (TCD) used to monitor the rate of $H_2$ consumption was calibrated prior to use using the reduction of AgO as a reference.

## 3. Results and Discussion

The iron oxide particles synthesized were shown by TEM analysis (Supplementary Material Fig. S1) to consist of crystalline particles with a range of sizes 2-10 nm. The methodology used [18] is intended to produce nanocrystals of $\gamma$-$Fe_2O_3$, we find that our selected area electron diffraction (SAED) and XRD spacings (Supplementary Material Fig. S2 and Table S1) support particles being either $\gamma$-$Fe_2O_3$ or $Fe_3O_4$ structure.

Two support materials have been investigated in this assemblage study. The materials have significant differences not only in chemical composition, but also in surface area and pore structures. The MCM-41 silicate used in this study has been characterized and discussed previously [7, 24, 25] and is comprised of a well ordered porous system. The alumina alternative, Puralox

SBa200, was supplied by SASOL. TEM imaging of Puralox SBa200 found the material consists of smaller crystals (~20 nm) that aggregate into larger clusters ~200-1000 nm in diameter. SAED and XRD (Supplementary Material Fig. S3) confirmed the $\gamma$-$Al_2O_3$ structure, with the predominant d-spacings measured. To ensure the support was fully dehydrated before assemblage of the particles, the support was calcined in air at 750 $^{o}$C. Using BET surface area measurements (Supplementary Material Table S2) we found that 2.5 hours calcination results in a slight decrease in surface area (185 to 162 $m^2$/g) but an increase in the pore diameter (75 to 84 Å), which should lead to greater impregnation of nanoparticles. TEM imaging revealed that calcination of materials for significantly longer than this resulted in a collapse of the material.

Both materials resulting from the assemblage of preformed iron oxide nanoparticles onto support materials were examined by TEM (Fig. 1). In the TEM image of Fe-MCM (Fig. 1(a)) highlights both the porous structure of the silicate and some nanoparticles across the surface; however, in the case of Fe-puralox (Fig. 1(b)) the nanoparticles cannot be differentiated from the small alumina crystals of the Puralox. The similar size of the pores and the particles make it unlikely that particles are contained inside the pores, it is more like that they are found exclusively on the support surface; however, the incorporation of some particles within the surface cannot be entirely ruled out. XRD and SAED could not be used to characterize the materials as the nanoparticles have a very low percentage incorporation (Table 1) and lead to a retention of bulk material. In both cases, but especially that of Fe-puralox, it is difficult to determine how well dispersed the nanoparticles are on the supports, leading to the requirement of further electron microscopy analysis.

The distribution of the iron oxide nanoparticles across Fe-MCM is more clearly demonstrated using high angle annular dark field scanning TEM (HAADF STEM) (Fig. 2 (a) and (b)), where the higher atomic number iron oxide nanoparticles appear much brighter than the silica support material. For Fe-MCM, we find particles are generally well distributed across the support material, only small amounts of clustering are found (Fig. 2b). The bright spots in the image are confirmed to be iron oxide through the use of EDX spectroscopy (Fig. 2 (c)), in which the analysed area from HAADF STEM contains both the K$\alpha$ and K$\beta$ signals of Fe. Variations in the thickness of the alumina aggregate in Fe-puralox limit the usefulness of HAADF STEM, and in this case we have used energy filtered TEM (EFTEM) to confirm the location of the preformed nanoparticles. Using EFTEM (Fig. 2 (d) and (e)), we can see that particles are found across the surface of the material, however they tend to occur as clusters rather than being fully distributed as in the Fe-MCM system and the previously studied FePt MCM-41 material.[5, 7] The clusters of nanoparticles are not large aggregates, rather individual particles that are packed closely together in a region of space, retaining their size. Further analysis of the Fe-puralox material found both areas of well distributed particles across the alumina surface (graphical abstract) and revealed some individual particles distributed across the surface next to a larger cluster (Fig. 3). Although it is known that nanoparticle composition and surfactant are important factors in determining the distribution; we also suggest that support type, appears to play an important role in determining the nanoparticle distribution.

In the FT process, catalysts are required to undergo multiple reduction and oxidation steps. It has been found that under heat treatment many metal cluster catalysts often do not retain their structure.[26] We find for our systems, that calcination of the catalysts did not result in a significant change in the materials appearance by TEM (Supplementary Material Fig. S4). There is no evidence of a loss in particle stability after either of the heat processes regardless of whether 200 $^{o}$C or 550 $^{o}$C was used. The distribution of the particles over the support following calcination is indistinguishable to the distribution prior to calcination. The $N_2$ adsorption and elemental analysis data for the calcined assembled materials is contained in Table 1. The addition of nanoparticles to puralox and MCM (Supplementary Material Table S2) results in only a subtle change to the surface area and pore diameter supporting the low percentage incorporation. The nanoparticles have maintained their shape and size during the assemblage and calcination processes. With the development of reliable synthetic procedures [27, 28] over the last decade allowing access to a range of transition and noble metal particles useful for catalysis using preformed nanoparticles in supported materials is readily achievable. Using these nanoparticles provides an avenue to more predictable samples than those obtained using traditional methods such as co-precipitation and sol-gel. The size of particles is known to affect catalytic activity,[29] and these materials allow access to more precisely size controlled materials suitable for particular catalytic regimes in addition to being useful for the study of size affects for more fundamental research.

The rate of assemblage regardless of support material was much slower than the previous work involving the assemblage of FePt nanoparticles onto MCM silicates.[5, 7] Reactions were deemed complete when the hexane became colorless. For the iron oxide materials, the solution was still highly coloured after six hours of stirring only becoming clear after being left overnight. For comparison, in the FePt system, the solution was fully decoloured in 90 minutes. [7] The composition and structure of support material played no role in altering the assemblage rate as two quite different materials were used yet no real difference was seen in how the particles assembled on the surface or the rate at which it occurs. Since the reactions were carried out in hexane, surface charge is unlikely to play a role in assemblage so we are left with the notion that nanoparticle structure or the coating is perhaps the determining factor in the process of assemblage. One feasible explanation involves the surface hydroxides/oxides on an iron oxide particle altering how the surfactants bind to the particle surface when compared to a particle of iron platinum. The changes in surfactant binding may alter the rates of assemblage. For FePt nanoparticles, the carboxylate head (COO-) of the oleic acid surfactant has been found to interact with Fe atoms via both mondentate and chelating bidentate (chelation of one Fe metal atom with COO-). [30] In the case of iron oxide, the interaction has been shown to proceed via both monodentate and bridging bidentate interaction (covalent bonding between two Fe metal atoms and a single COO- group) [31] One can envisage that these differences in the surface coating could affect the rate of assemblage.

The reductive behavior of the catalysts has been studied by $H_2$-Temperature Programmed Reductions (TPR). Iron oxides are known to have lower FT activity than the zero valent iron materials. Indeed, iron compounds used in FT are converted to $Fe_3O_4$ in the absence of sulfur.[32] Catalysts as a result are required to undergo subsequent reduction cycles during catalysis so they are reactivated. When using preformed nanoparticles it is more feasible to work with air stable iron oxide nanoparticles and subsequently reduce these to iron. The reducibility of the nanocataylsts is interpreted through both TPR profiles and TGA (Fig. 4).

The shape of the TPR curves for Fe-MCM and Fe-puralox appear to be complicated in form. Similar profiles have been seen previously for other iron containing catalysts.[33] Several regions of interest are distinguished for these materials by the peaks in the TCD signal. Generally, the profiles for Fe-MCM and Fe-puralox are similar, with the exception of a peak in Fe-puralox centred at around 230 $^{o}$C. This peak is likely to be the result of the surface reduction of oxides and removal of –OH groups as seen in other iron alumina materials.[33] In both materials we see a peak in the TPR profile below 100 $^{o}$C. This can is attributed to the desorption of physisorbed water contained in the support material.

The main feature of the Fe-MCM and Fe-puralox profiles is a series of overlapping peaks with the maximum occurring at around 530 $^{o}$C for Fe-MCM and 500 $^{o}$C for Fe-puralox. These peaks correspond to the maximum rate of reduction for the iron oxide particles. The complexity of the TPR profiles is likely to arise from a multistep reduction process of the iron oxide. [34, 35] In this process, $Fe_2O_3$ particles would first be reduced to $Fe_3O_4$ at around 350-400 $^{o}$C. Subsequently, these are reduced to FeO that is in turn reduced to Fe. The reduction to Fe is more difficult and normally over a large temperature range (500-750 $^{o}$C). Only two peaks are normally found in the TPR profile of iron oxide as the conversion of FeO to Fe is rapid. [34, 35] We find that two reduction regions are seen in Fe-MCM and Fe-puralox profiles contained in Fig. 4. It seems likely that although our SAED and XRD cannot confirm the structural phase of our iron oxide particles to be either $\gamma$-$Fe_2O_3$ or $Fe_3O_4$, TPR and TGA suggest a reductive behavior consistent with the occurrence of at least some $\gamma$-$Fe_2O_3$.

In addition to the multistep reduction process, the nanoparticle size distribution appears to have altered the TPR profile. The low temperature reduction of $Fe_2O_3$ to $Fe_3O_4$ seems to be comprised of overlapping peaks (360-490 $^{o}$C). Slight changes in particle size is known to affect the temperature at which reduction occurs.[36] A recent study found that subtle changes in size (5.9-12.5 nm) of $Co_3O_4$ nanoparticles lead to shifts in the reduction temperature by a significant amounts; $Co_3O_4$ to CoO by 65 K and CoO to Co by 135 K.[37] It has been seen for other iron oxide supported catalysts that have a similar particle distribution to the particles used in this work the TPR profile had two peaks observed for the $Fe_2O_3$ reduction while only a single peak was noted for the full reduction to iron. [38]

Thermal decomposition of the calcined samples was studied by TGA in an 8% $H_2$ in $N_2$ gas mixture to allow more accurate interpretation of the TPR. There are three main regions of weight loss, for both materials;

(i)<250 $^oC$ desorption of physisorbed water leads to minor mass decrease; a more significant decrease is noted in the alumina sample due to surface reduction of oxides and removal of –OH

(ii)250-550 $^oC$ reduction of $Fe_2O_3$ to $Fe_3O_4$

(iii) > 500 $^oC$ reduction of the iron oxide reduction of $Fe_3O_4$ to Fe

Iron systems are well known to require high temperatures for reduction. Indeed the full reduction of $Fe_2O_3$ has to $Fe^0$ has been reported to occur at 650 $^oC$ via an intermediate reduction of $Fe_2O_3$ to $Fe_3O_4$ at 350 $^oC$.[34, 35] It has been suggested that the porous structure of MCM materials may begin to breakdown at the temperatures required for reduction.[39] Full reduction for Fe-MCM is not achieved to around 650 $^oC$; however, at temperatures above 600 $^oC$ it is known that damage to the MCM-41 structure can occur.[39]

## 4. Conclusions

The ability to synthesize particles before assemblage onto a support allows a greater control over system features. It is well know that particle size and dispersion has implications for catalyst properties. Nanoparticles formed in-situ by the reduction of metal salts on the surface of support materials are less easily fine-tuned than preformed systems. This project is an extension of our earlier studies into the assemblage of preformed nanoparticles over silica. In this case we have investigated the use of iron oxide nanoparticles and assembled these onto both alumina and silica supports for use as FT catalysts. We have found that the particles adhere well to the support materials and are stable after calcination. The distribution across the supports is varied with iron oxide particles dispersing better on silica supports than those containing alumina. Further work is required to ascertain if the distribution of preformed nanoparticles on silica supports is restricted to iron based systems or more widely available to other metals of interest. Despite the relatively good dispersion seen for iron oxide particles on MCM-41, the high temperatures required for reduction could damage the support material. Fe-MCM would possibly not be suited to repeated oxidation-reduction cycles as loss of support structure will inevitably lead to particle aggregation. Although a poorer distribution of nanoparticles was seen over the alumina support, the material is much more suited to multiple reduction steps. Future investigations will involve testing the Fisher-Tropsch catalytic performance of the two catalysts and compare these to materials synthesized by wet impregnation method.

## Acknowledgments

The authors acknowledge the facilities, scientific and technical assistance of the Australia Microanalysis Research Facility at the Centre for Microscopy, Characterisation & Analysis, The University of Western Australia, a facility funded by The University, State and Commonwealth Governments. NH would like to thank the University of Leeds for a World Universities Network Research Mobility Programme award. ROF would like to thank the University of Western Australia for a research development award, Prof. P. McCormick for use of TriStar II 3020, W/Prof. D. k. Zhang and Mr Z. Zhang for use of the TA SDT Q600 and Prof. G. Koutsantonis for use of the Autochem II 2920.

## References

1. A. Gual; C. Godard; S. Castillón; D. Curulla-Ferré; C. Claver, *Catal. Today* **2012,** 183, 154-171.
2. Y. Zhu; L. P. Stubbs; F. Ho; R. Liu; C. P. Ship; J. A. Maguire; N. S. Hosmane, *ChemCatChem* **2010,** 2, 365-374.
3. A. Alayoglu; S. K. Beaumont; F. Zheng; V. V. Pushkarev; H. Zheng; V. Iablokov; Z. Liu; J. Guo; N. Kruse; G. A. Somorjai, *Top. Catal.* **2011,** 54, 778-785.
4. T. Hyeon, *Chem. Commun.* **2003**, 927-934.
5. R. O. Fuller; N. S. Hondow; G. A. Koutsantonis; M. Saunders; R. L. Stamps, *J. Phys. Chem. C* **2008,** 112, (14), 5271-5274.
6. A. F. Gross; M. R. Diehl; K. C. Beverly; E. K. Richman; S. H. Tolbert, *J. Phys. Chem. B* **2003,** 107, (23), 5475-5482.
7. N. S. Hondow; G. A. Koutsantonis; R. O. Fuller; H. Fansuri; M. Saunders; R. L. Stamps; D. Zhang, *New. J. Chem.* **2010,** 34, 1286-1294.
8. J.-l. Shi; Z.-l. Hua; L.-x. Zhang, *J. Mater. Chem.* **2004,** 14, (5), 795-806.
9. S. Sun; C. B. Murray; D. Weller; L. Folks; A. Moser, *Science* **2000,** 287, 1989-1992.
10. D. P. Dinega; M. G. Bawendi, *Angew. Chem. Int. Ed.* **1999,** 38, (12), 1788-1791.
11. G. L. Bezemer; P. B. Radstake; V. Koot; A. J. van Dillen; J. W. Geus; K. P. de Jong, *J. Catal.* **2006,** 237, (2), 291-302.
12. J. Guzman; B. C. Gates, *Dalton Trans.* **2003**, 3303-3318.
13. R. C. Reuel; C. H. Bartholomew, *J. Catal.* **1984,** 85, (1), 78-88.
14. E. Iglesia; S. L. Soled; R. A. Fiato, *J. Catal.* **1992,** 137, (1), 212-224.
15. A. Barbier; A. Tuel; I. Arcon; A. Kodre; G. A. Martin, *J. Catal.* **2001,** 200, (1), 106-116.
16. B. G. Johnson; C. H. Bartholomew; D. W. Goodman, *J. Catal.* **1991,** 128, (1), 231-247.

17. G. L. Bezemer; J. H. Bitter; H. P. C. E. Kuipers; H. Oosterbeek; J. E. Holewijn; X. Xu; F. Kapteijn; A. J. van Dillen; K. P. de Jong, *J. Am. Chem. Soc.* **2006,** 128, (12), 3956-3964.
18. T. Hyeon; S. S. Lee; J. Park; Y. Chung; H. B. Na, *J. Am. Chem. Soc.* **2001,** 123, 12798-12801.
19. S. Sun; H. Zeng; D. B. Robinson; S. Raoux; P. M. Rice; S. X. Wang; G. Li, *J. Am. Chem. Soc.* **2004,** 126, 273-279.
20. M. A. Morales; A. J. S. Mascarenhas; A. M. S. Gomes; C. A. P. Leite; H. M. C. Andrade; C. M. C. de Castilho; F. Galembeck, *J. Coll. Interf. Sci.* **2010,** 342, (2), 269-277.
21. S. Ayyappan; S. Mahadevan; P. Chandramohan; M. P. Srinivasan; J. Philip; B. Raj, *J. Phys. Chem. C* **2010,** 114, (14), 6334-6341.
22. V. F. Puntes; D. Zanchet; C. K. Erdonmez; A. P. Alivisatos, *J. Am. Chem. Soc.* **2002,** 124, (43), 12874-12880.
23. D. Kumar; K. Schumacher; C. du Frensne von Hohenesche; M. Grun; K. K. Unger, *Colloids Surf. A* **2001,** 187-188, 109-116.
24. C. T. Kresge; M. E. Leonowicz; W. J. Roth; J. C. Vartuli; J. S. Beck, *Nature* **1992,** 359, 710-712.
25. J. S. Beck; J. C. Vartuli; W. J. Roth; M. E. Leonowicz; C. T. Kresge; K. D. Schmitt; C. T.-W. Chu; D. H. Olson; E. W. Sheppard; S. B. McCullen; J. B. Higgins; J. L. Schlenker, *J. Am. Chem. Soc.* **1992,** 114, 10834-10843.
26. D. F. Shriver; H. D. Kaesz; R. D. Adams, *The chemistry of metal cluster complexes*. VCH Publishers, Inc.: New York, 1990.
27. B. L. Cushing; V. L. Kolesnichenko; C. J. O'Connor, *Chem. Rev.* **2004,** 104, (9), 3893-3946.
28. J. P. Wilcoxon; B. L. Abrams, *Chem. Soc. Rev.* **2006,** 35, (11), 1162-1194.
29. M. Haruta, *Catal. Today* **1997,** 36, (1), 153-166.
30. S. Sun, *Adv. Mater.* **2006,** 18, (4), 393-403.
31. L. Zhang; R. He; H.-C. Gu, *Appl. Surf. Sci.* **2006,** 253, (5), 2611-2617.
32. T. Suzuki; O. Yamada; Y. Takahaski; Y. Watanabe, *Fuel Proc. Tech.* **1985,** 10, 33-43.
33. T. V. Reshetenko; L. B. Avdeeva; A. A. Khassin; G. N. Kustova; V. A. Ushakov; E. M. Moroz; A. N. Shmakov; V. V. Kriventsov; D. I. Kochubey; Y. T. Pavlyukhin; A. L. Chuvilin; Z. R. Ismagilov, *Appl. Catal., A* **2004,** 268, (1–2), 127-138.
34. A. J. H. M. Kock; H. M. Fortuin; J. W. Geus, *J. Catal.* **1985,** 96, (1), 261-275.
35. D. B. Bukur; K. Okabe; M. P. Rosynek; C. P. Li; D. J. Wang; K. R. P. M. Rao; G. P. Huffman, *J. Catal.* **1995,** 155, (2), 353-365.
36. D. Kumar; S. Varma; N. M. Gupta, *Catal. Today* **2004,** 93–95, (0), 541-551.
37. G. Prieto; A. Martínez; P. Concepción; R. Moreno-Tost, *J. Catal.* **2009,** 266, (1), 129-144.
38. W. Chen; Z. Fan; X. Pan; X. Bao, *J. Am. Chem. Soc.* **2008,** 130, (29), 9414-9419.
39. M. Broyer; S. Valange; J. P. Bellat; O. Bertrand; G. Weber; Z. Gabelica, *Langmuir* **2002,** 18, (13), 5083-5091.

## Tables

| Sample | BET Surface Area ($m^2/g$) | BJH Desorption pore diameter (Å) | Aluminium weight % | Silicon weight % | Iron weight % |
|---|---|---|---|---|---|
| Calcined 200 $^oC$ Fe-MCM | 709 | 25 | .05 | 27.8 | 1.87 |
| Calcined 550 $^oC$ Fe-MCM | 1074 | 27 | - | - | - |
| Calcined 200 $^oC$ Fe-puralox | 159 | 83 | 47.2 | .44 | 1.45 |
| Calcined 550 $^oC$ Fe-puralox | 154 | 123 | - | - | - |

Table 1: Textural properties of the nanocatalysts

## Figures

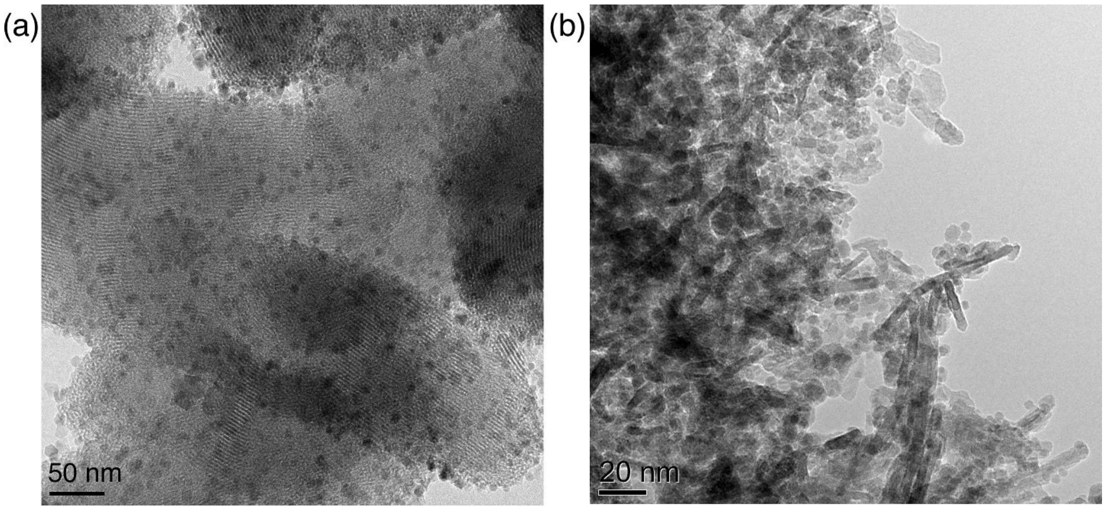

Fig. 1: Bright field TEM images of (a) Fe-MCM and (b) Fe-Puralox. Whilst both the pore structure and nanoparticles are evident in the TEM image of Fe-MCM, the crystalline nature and small crystal size of Puralox make it indistinguishable from the iron oxide nanoparticles.

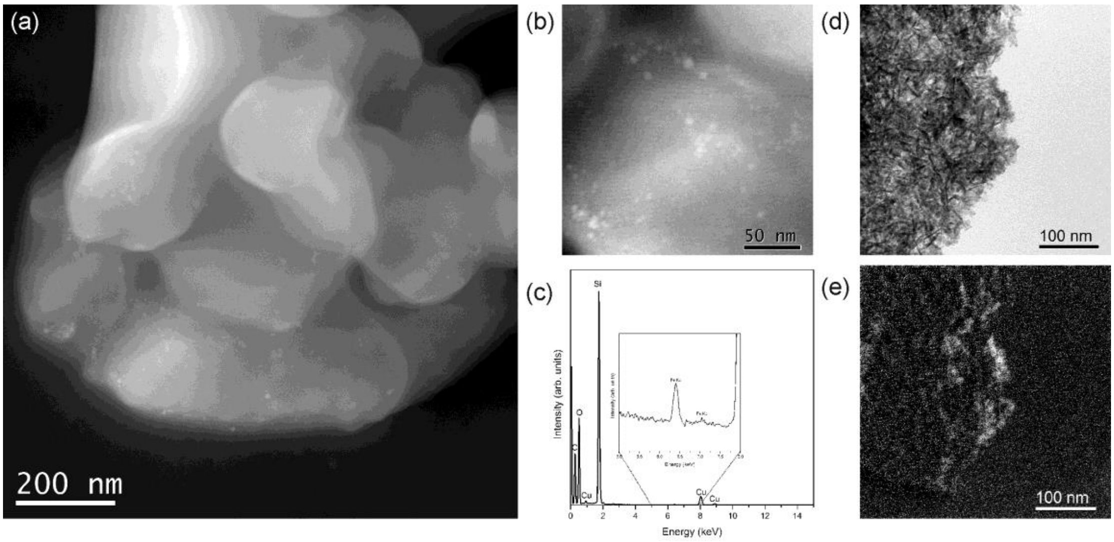

Fig. 2: Further electron microscopy of the assembled materials; (a) HAADF STEM image of Fe-MCM in which the distribution of the nanoparticles is highlighted by atomic contrast, (b) higher magnification HAADF STEM image of Fe-MCM in which both the nanoparticles and pores are viewed, (c) EDX analysis of the region in (b), (d) bright field TEM image of Fe-puralox in which the puralox particles cannot be distinguished from the iron oxide, and (e) corresponding Fe *L* EFTEM map of Fe-puralox in which the iron oxide particles are clearly identified.

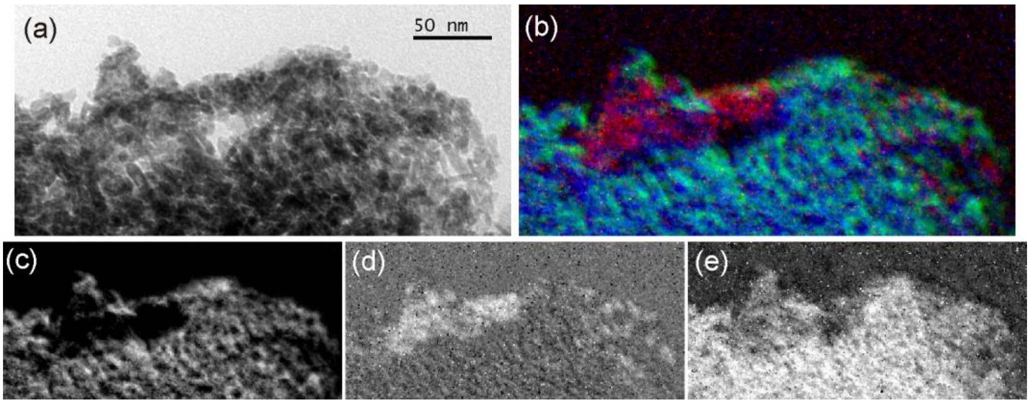

Fig. 3**:** Energy Filtered TEM was used to determine the distribution of elements in the Fe-puralox material. (a) Bright field TEM image; (b) false coloured elemental map where aluminium is green, iron is red and oxygen is blue; (c) aluminium *L* map; (d) iron *L* map; and (e) oxygen *K* map. These EFTEM maps show that the iron oxide exists as both clusters and dispersed particles.

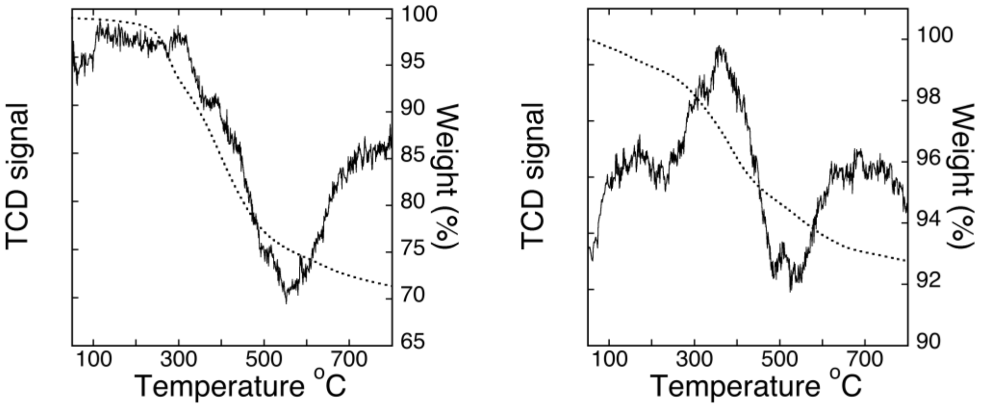

Fig. 4: The $H_2$-TPR profiles (solid) and TGA (dotted) for calcined Fe-MCM (left) and calcined Fe-puralox (right).